Journal of Alloys and Compounds 1065 (2026) 188288

Contents lists available at ScienceDirect

Journal of Alloys and Compounds

journal homepage: www.elsevier.com/locate/jalcom

Effect of Si content on the thermal response and stability of Al-40Sn-XSi-Mg composite PCMs

S. Marola [a,*], M. Molteni [a], P. Bassani [b], E. Gariboldi [a]

[a] Politecnico di Milano, Department of Mechanical Engineering, Via la G. La Masa 1, Milano 20156, Italy
[b] National Research Council of Italy, Institute of Condensed Matter Chemistry and Technologies for Energy, CNR-ICMATE, Via Previati 1/E, Lecco 23900, Italy

ARTICLE INFO

Keywords:
Metallic phase change materials
(Al–Si–Sn) alloys
Thermal diffusivity
Microstructural stability
Latent heat
Specific heat

ABSTRACT

Metallic Phase Change Materials (m-PCMs) are gaining interest for medium-temperature thermal energy storage due to their high thermal conductivity, mechanical robustness, and chemical stability. Prior studies showed that adding 40_{mass}%Sn to Al and commercial Al–Si alloys yields effective composite m-PCMs, where Sn provides high latent heat and the Al/Al–Si matrix ensures dimensional stability during cycling. Building on this concept, this work examines the thermal response and stability of Al-40Sn, Al-40Sn-3Si-Mg and Al-40Sn-4Si-Mg alloys to clarify how the Si content affects the overall thermal behavior. Induction-melted ingots were characterized through microstructural analysis, Differential Scanning Calorimetry, and Laser Flash Analysis in the as-produced state and after thermal cycling across the activation temperature. Measured latent heat, specific heat capacity, and thermal diffusivity were compared with equilibrium thermodynamic simulations to evaluate the influence of Si on thermal response and cycling stability. Results show that varying Si from 0 to 4_{mass}% does not significantly affect the melting temperature and the latent heat associated with Sn melting, while it modifies the temperature spread of the phase transition through secondary Mg_2Sn–Sn eutectic reaction. Si additions strongly enhance microstructural stability during cycling by improving Sn confinement within the Al–Si matrix and limiting porosity evolution. Consequently, the phase-change thermal response remains highly reproducible, and thermal diffusivity is markedly more stable than in the Al–Sn system. These findings clarify how composition, microstructure, and porosity jointly govern the thermal performance of Al-Sn-Si-Mg m-PCMs, providing guidelines for efficient and durable thermal energy storage materials.

1. Introduction

Immiscible metallic systems, i.e. systems made up by at least two different metals, which do not lead to the formation of homogeneous solid solutions [1], have recently attracted the attention of the research world due to their outstanding property combinations, leading to self-lubricant, high thermally and electrically conductive materials [2] or even combining magnetic and highly corrosive resistant behavior [3]. Indeed, the presence of miscibility gaps either at the thermodynamic equilibrium [4] or in metastable conditions [5], leads to the formation of in-situ metal matrix composites [6]. The very limited reciprocal solubility of the elements in an immiscible system indeed, in addition to the scarce interaction between them, provides phases whose composition roughly coincides with the one of pure metals. Owing to these peculiar features, immiscible metallic systems are currently considered for a broad range of applications. For instance, Cu-based systems combined with Fe are employed in high-heat-flux applications such as power generation systems and heat exchangers [7], while Nb [8] or Ag [9,10] can also be added to Cu for similar purposes. Moreover, Cu-Ag combinations have additionally been explored for biomedical applications [11]. Cu can also be combined with W [12] for aerospace, military, and electronics-related fields, or with Bi for soldering purposes [13]. Likewise, Mo-based immiscible systems have been proposed for high-temperature applications when combined with either Si [14] or Cu [15]. Al-based immiscible alloys, such as Al-Sn [16], Al-Pb [17,18], and Al-Bi [19], are instead well known for anti-friction applications, where Al acts as a load-bearing matrix and the secondary phases provide solid-lubricating action.

Recently, Al-based alloys have also emerged as promising candidates for Thermal Energy Storage/Thermal Management (TES/TEM) applications, either as active PCM (especially for Al-Si systems), or as supporting load-bearing matrix for containing PCM when liquid. Whereas

* Corresponding author.
E-mail address: silvia.marola@polimi.it (S. Marola).

https://doi.org/10.1016/j.jallcom.2026.188288
Received 27 February 2026; Received in revised form 9 April 2026; Accepted 26 April 2026
Available online 27 April 2026

Al-Si alloys have been widely studied as metallic PCMs for medium- to high-temperature service, such as concentrated solar power, generally in combination with micro-encapsulation strategies to ensure chemical stability and suppress leakage [20,21], immiscible Al-based alloys represent a promising alternative for lower/intermediate-temperature applications. As composite PCMs, they can bridge the gap between conventional low-temperature metallic PCMs and higher-temperature Al-Si-based systems [22]. In this regard, Al-Sn alloys [23] have attracted increasing interest for TES/TEM purposes [24,25], by virtue of their metastable miscibility gap [5]. Specifically, in these composite PCMs, the low melting point element, i.e. Sn (with melting temperature T_m = 232°C) works as PCM [26], whereas Al (T_m = 660°C) covers the role of the matrix, within which Sn is dispersed. Accordingly, the Al-Sn system should be regarded not as a fully active metallic PCM, but as a composite material, in which the low-melting phase is responsible for latent heat storage, while the Al-rich matrix provides thermal conduction and mechanical containment. Sn transition temperature indeed, combined with its relatively high latent heat of fusion per unit mass, makes it appealing for the management of low grade waste heat (up to 232°C). This latter, notwithstanding represents the 60% of the total waste heat, is the most difficult to recover, due to the lack of technical solutions within this specific temperature range [27]. More generally, PCMs exploit their latent heat of transformation to store and accumulate thermal energy at an almost constant temperature, namely that of the phase transition, to release it during the reverse transformation [28]. Among the different transformation mechanisms, the solid-liquid transition is the most widely exploited, as it offers the best compromise between the manageable volume variation associated with the phase change and the amount of storable heat. In Al-Sn systems, the Al matrix acts mainly as a containment medium and heat transfer enhancer, preventing possible leakage of molten Sn or undesired side reactions [29], while at the same time promoting an efficient heat conduction toward the active PCM.

Other secondary elements that do not modify the immiscible nature of the Al-Sn system such as Si or Cu can also be added [30]. These additions have been shown to enhance the performances of the Al-Sn alloys both in terms of wear resistance [31] and PCM behavior [32]. In particular, in Al-Si-Sn systems, Si contributes to maintaining the immiscible character of the alloy while reinforcing the Al-based supporting matrix. Accordingly, the Al-Si framework promotes phase confinement, efficient thermal conduction, and enhanced mechanical integrity and structural stability of the composite PCM architecture.

However, it is worth mentioning that metallic immiscible systems proper functioning is strictly related to the production technology and, consequently, the achieved microstructure. Indeed, during conventional sand casting procedure, these alloys usually suffer of strong segregation effect of the minor elements, which can act as a weak point of the system. The microstructure formation is mainly related to the diffusion of the solute in the matrix. In case of casting production methods, the immiscible nature of the alloys, can lead to a liquid-liquid separation and the consequent formation of droplets, which tend to coalesce due to both Stokes sedimentation, held by gravity, and Marangoni motion, run by temperature/concentration gradients [1,4,7]. On the other hand, a homogeneous dispersion of the minor element within the matrix is desired in order to obtain target properties [24]. The employment of powder metallurgy routes [17,33] or the application of either electric/magnetic fields [4,34] or ultrasounds [35] to the molten alloy in this sense demonstrate to promote a much more efficient control of the microstructure, avoiding the coalescence of minor phases. These techniques have been successfully applied to the production of Al-Sn systems [36,37]. Besides these methods, imposing high or controlled cooling rates to the melt is an effective approach for the production of bulk materials [38–40] or coatings [41,42].

In this view, the majority of the literature concerning Al-Sn usually focuses on systems with limited amount of Sn, 10_{mass}% is rarely exceeded, specifically addressed toward wear resistant applications. On the other hand, for PCM purposes, the increase of Sn amount can improve the energy storage potential of the system in terms of latent heat of fusion, being the two quantities proportional. Moreover, to the authors' best knowledge, notwithstanding the crucial role of the temperature-dependent thermophysical properties for the PCM performance evaluation, the current literature is still limited in terms of experimental data [25,32]. Besides the evaluation of latent heat of fusion, also physical quantities such as specific heat, determining the sensible heat storage capability, or thermal conductivity, strictly related to the PCM response fastness, are essential for the effectiveness evaluation of PCMs [22,43]. In this sense, Manasijevic et al. [25] characterized both microstructure and thermophysical properties varying the quantity of Sn to be added to Al, employing casting with stainless steel mold, whereas some of the authors already tested water granulated Al+ 40_{mass}%Sn mass and A356 (AlSi7Mg)+ 40_{mass}%Sn mass products [32]. In this sense, the modification of the composite composition can consequently affect the thermophysical properties of the resulting system. The authors indeed, in [32], experimentally stated that the employment of A356 alloy in combination with Sn, modified PCM transition temperature, spreading the low-melting phase melting temperature from 230°C of Sn in the bare Al-Sn system to 200–230°C interval. This behavior is related to the presence of small traces of Mg, already present in the base A356, which led to the formation of low-melting eutectic involving Mg_2Sn and Sn.

Chemical composition changes with respect to the bare Al-Sn system can also have an impact on the other thermophysical properties of interest for PCMs. The authors indeed, recently showed with the means of CALPHAD-based and analytical model calculations, the effective thermal conductivity (essential for the determination of the system response fastness) of the Al+ 40_{mass}%Sn and A356 + 40_{mass}%Sn systems within RT-700°C range [44]. The results showed a reduction in the effective thermal conductivity for the A356 + 40_{mass}%Sn system with respect to the bare binary system due to the introduction of other alloying elements. This statement is also experimentally confirmed for instance for commercially Al-based alloys in general [45,46]. However, to the authors' best knowledge, their impact on the thermal transport properties for high-Sn bearing Al-based alloys is yet to be fully clarified.

Moreover, it is worth mentioning that also the technology-related defects, such as porosities, have an impact on the thermophysical and heat storage properties of the composite PCMs [47], as well as the arrangement of the phases within the microstructure [48]. However, the current literature still lacks a systematic analysis on the thermophysical properties resulting from the interplay of all the listed factors for the selected systems.

Despite recent advances in Al-Sn-based composite PCMs, the combined influence of alloy composition, casting-induced microstructural features, and resulting thermophysical behavior is still not fully understood. In this context, the present work explores the use of commercially available Al/Al-Si casting alloys added with 40_{mass}%Sn as composite metallic PCMs for intermediate-temperature thermal energy storage applications. In these systems, the Sn-rich phase provides the latent-heat storage contribution, whereas the Al-based matrix ensures thermal conduction, phase confinement, and structural stability. This strategy is relevant not only for filling an intermediate application-temperature window, but also from a sustainability perspective, as it opens the possibility of exploiting readily available casting alloys, opening future possibilities for the use of recycled or scrap-derived feedstock, instead of relying on specifically engineered Al-Sn-based alloys. Therefore, the present study aims to assess how Si content and graphite-mold casting affect microstructure, defect formation, and thermophysical response, while also evaluating the potential of recyclable casting-grade alloys as durable and industrially viable metallic composite PCMs. By coupling detailed experimental characterization with CALPHAD-based thermodynamic modelling, this work clarifies how microstructural features, secondary phases, and porosity jointly affect the thermal response and cycling stability of Al–SiX+ 40_{mass}%Sn (X = 0–4_{mass}%) composite PCMs. The results provide new insight into the design of compositionally optimized, durable metallic PCMs for intermediate-temperature thermal

energy storage applications.

2. Materials and methods

2.1. Ingot production

The chemical compositions of the investigated alloys belonging to the Al–40$_{mass}$%Sn and Al–XSi-40$_{mass}$%Sn (X = 0–4$_{mass}$%) systems is reported in Table 1, together with their reference name, related to the target Si content. The Si levels examined in this work (3.07 and 4.09$_{mass}$%) were selected to represent compositions closer to conventional Al-Si casting alloys rather than specifically designed bearing alloys. This choice was intended to explore matrix materials of greater industrial relevance and recycling potential, while also assessing the effect of a moderate Si increase on the stability of the Al-based supporting matrix.

The alloys were produced by induction melting in a graphite crucible (VCMIII model, Aseg Galloni), under Ar flux. As far as the charge material is concerned, 40$_{mass}$% commercially pure Sn, together with AlSiMg(Fe) foundry alloys, were used to obtain the targeted Si content. These commercial Al-Si casting alloys were deliberately selected as matrix-forming materials in order to investigate technologically relevant compositions instead of highly purified or specially prepared laboratory alloys. As a result, the final materials contained not only Si but also minor alloying elements typically found in casting alloys, such as Mg, Mn, and Fe; their contents are also reported in Table 1.

After completion of the melting procedure, the molten metal was cast in a graphite mold of 90 × 70 × 12 mm^3 size. The latter was preheated to get rid of possible moisture or other contaminants. After completion of the casting, the ingots were extracted from the mould, the feeding channel was removed and the resulting ingot sectioned according tests requirement. Hereafter the alloys will be referred as Al-40Sn or Al-40Sn-XSi-Mg, where X corresponds to their Si content.

2.2. Sampling and specimen preparation

A schematic illustration of the sampling strategy is shown in Fig. 1. Specimens for thermal and microstructural characterization were extracted from regions of each ingot. Samples nominally measuring 5 × 5 × 12 mm^3, taken from the bottom part of the ingot (red samples in Fig. 1), were prepared for microstructural investigations. Specimens for thermal diffusivity tests measuring 10 × 10 x 2.5 mm^3 (blue specimens) were instead taken from the innermost part of the ingots to avoid potential effects of segregation or microstructural directionality, ensuring reliable measurements of thermal properties representative of the bulk material. The same inner region was selected for differential scanning calorimetry and specific heat capacity samples, whose masses oscillate around 50 mg.

Part of the samples were subjected to 10 thermal cycles in order to preliminarily assess the early-stage alloys stability and interpret their thermal response in light of thermodynamic predictions. Thermal cycles of metallographic and thermal diffusivity specimens were performed between 25 °C and 270 °C under vacuum, at a heating rate of 2 °C/min to ensure uniform temperature distribution within the specimen.

Specimens for metallographic observations were prepared following a standard polishing procedure. After sequential grinding with SiC papers up to P2500 grit, samples were polished with 6, 3, and 1 μm diamond suspensions, followed by a final polishing step with 10% colloidal silica dispersion in distilled water.

Table 1
Nominal chemical composition of the investigated ingots (in $_{mass}$%).

	Al	Si	Mg	Fe	Mn	Sn
Al-40Sn	Bal.	0.004	0.001	0.001	-	39.98
Al-40Sn-3Si-Mg	Bal.	3.07	0.11	0.17	0.09	39.99
Al-40Sn-4Si-Mg	Bal.	4.09	0.15	0.22	0.13	39.99

2.3. Thermal characterization

DSC measurements were carried out to determine the transition temperature range, enthalpy, and specific heat capacity of the Al–Si–Sn composites. Each sample was subjected to ten thermal cycles between 100 °C and 300 °C at a constant heating/cooling rate of 20 °C/min. An isothermal dwell of 15 min was applied at both temperature limits to ensure thermal stability and repeatability. All tests were performed in Al_2O_3 crucibles under a continuous argon flow of 20 ml/min. The specific heat capacity at constant pressure was evaluated according to ISO 11357–4:2021 using the continuous-scanning method. The specific heat capacity of the alloys (C_p^{sp}) was calculated from DSC measurements according to:

$$C_p^{sp} = C_p^{cal}\frac{m^{cal}(P_{sp} - P_{bl})}{m^{sp}(P_{cal} - P_{bl})} \quad (1)$$

in which C_p is the specific heat capacity in J/(g•K), m is the mass of the sample in g, P is the heat flow rate (dQ/dt) in W. The subscript/superscript sp represents the specimen, bl refers to the blank run, and cal to the calibration material (here α-alumina, sapphire).

Thermal diffusivity was measured under vacuum using a Laser Flash Analyzer in the 20–300 °C temperature range. The metallic samples were prepared from the bulk material by precision cutting and machined into disk-shaped specimens with a diameter of 10 mm and a nominal thickness of 2.5 mm. Both surfaces were progressively ground with SiC abrasive papers up to P2500 in order to obtain smooth and planar faces. The specimen thickness was measured with a caliper by performing at least five measurements at different positions on each sample, and the average value was used for data analysis. Before testing, a thin graphite coating was sprayed on both sample surfaces to improve laser absorption and infrared emissivity during the LFA measurements. No temperature-related thickness correction was applied, since within the investigated temperature range the contribution of thermal expansion was considered limited; the overall estimated error, including both experimental uncertainty and thermal expansion effects, was approximately 2.4%, consistent with the instrumental uncertainty declared by the manufacturer of the equipment. Thermal diffusivity values were calculated using the combined correction model implemented in the Linseis software, and each reported data point represents the average of three laser shots, presented as mean value ± standard deviation. Data were acquired every 20 °C during both heating and cooling cycles, setting a heating rate of 5 °C/min. LFA measurements were performed during the 1st and the 10th thermal cycles, while the intermediate cycles were carried out in a tubular furnace under flowing Ar (50 ml/min), adopting the same heating and cooling rate used for the LFA measurements (5 °C/min). Measurements up to 300 °C were performed using a graphite-sapphire sample holder designed for liquid material. Compared with a conventional graphite holder, the graphite–sapphire holder yielded thermal diffusivity values that were systematically lower, corresponding to an average underestimation of approximately 23%. This deviation was quantified by calibration against the standard (solid) configuration at temperatures below the melting point of Sn (Figure S1 in Supplementary information). The reported thermal diffusivity values were corrected accordingly.

2.4. Microstructural characterization

Microstructural analyses were first conducted by optical microscopy on both as-cast and cycled specimens to assess the homogeneity and stability of the microstructure after thermal cycling. Porosity was quantified by image analysis using ImageJ software on at least 10 micrographs per sample (at magnification as in Fig. 2), acquired from multiple distinct regions of the ingot to ensure spatial

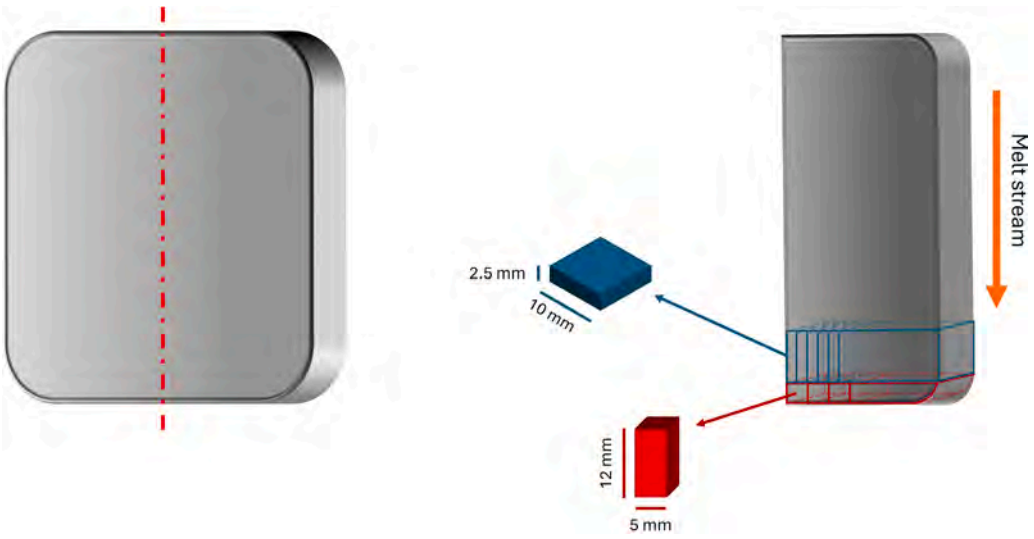

Fig. 1. Schematic representation of how samples were extracted from the ingots. Red-colored samples are used for microstructural analyses, blue-ones for thermal diffusivity measurements. Small size specimens for DSC tests were sampled close to thermal diffusivity samples.

representativeness.

For higher magnification observations and compositional analysis, a field emission scanning electron microscope equipped with an Energy Dispersive X-ray Spectroscopy (EDS) detector was used. Secondary and backscattered electron imaging, combined with EDS, were performed in multiple regions of the ingot to assess microstructural and compositional stability after thermal cycling.

2.5. Thermodynamic simulations

Thermodynamic simulations were performed under equilibrium conditions using Thermo-Calc 2024b software coupled with the TCAL8 v8.2 database. The nominal compositions of the ingots were used as input for the calculations. The resulting thermodynamic and phase stability predictions were compared with the experimental data in order to assess the reliability of Thermo-Calc as a predictive tool and to evaluate its potential for guiding the design and development of new composite PCMs.

3. Results and discussion

3.1. Microstructural features and Thermo-Calc predictions

Fig. 2 shows optical micrographs of the investigated ingots, including Al-40Sn, Al-40Sn-3Si-Mg and Al-40Sn-4Si-Mg, all in the as-produced condition and after 10 thermal cycles between 25 and 300°C. The microstructural observations are first presented for the as-produced condition and then discussed after thermal cycling to highlight the effect of cycling on each alloy system more compactly.

3.1.1. Al-40Sn alloy

In the as-cast Al-40Sn alloy, the microstructure is composed of Al dendrites and Sn regions that are essentially pure (top left in Fig. 2 and top row in Fig. 3), consistent with the very limited mutual solubility of Al and Sn [23]. The as-produced material exhibits a porosity of approximately 4 ± 1 $_{vol}$%, as determined by optical analyses.

After thermal cycling, a marked coarsening of the Al dendritic network is observed (top right in Fig. 2 and top row in Fig. 4), accompanied by a redistribution of Sn into pockets within the Al-rich zones forming a surrounding interconnected network, consistently with previous literature results [49]. This microstructural rearrangement can be related to liquid metal corrosion of Al by Sn, which preferentially attacks the grain boundaries [50], while the presence of spherical Sn features can be related to Rayleigh's instability phenomena [51]. Following 10 thermal cycles, the measured porosity increases to about 8 ± 1 $_{vol}$%, in agreement with the mass variation measured after thermal cycling (Table 2). These two pieces of evidence consistently support the occurrence of partial leakage of the Sn-rich liquid phase during repeated melting/solidification. The extent of such leakage is reasonably associated with the volume fraction and interconnection of the Sn-rich regions exposed to the sample surface, which may promote the formation of well-defined droplets when the exposure occurs in air [52]. This behavior is consistent with literature reports [53,54] showing poor wetting of solid Al_2O_3, inherently present as a native oxide on pure Al, by molten Sn and high liquid–solid interfacial angles, which reduce capillary retention and favor the escape of the Sn-rich liquid phase during repeated melting–solidification cycles.

3.1.2. Al-40Sn-3Si-Mg and Al-40Sn-4Si-Mg alloys

The introduction of Si and other minor alloying elements in the alloy composition results in the formation of an additional Al–Si eutectic phase alongside the pure Al and Sn phases. This eutectic is primarily located in the interdendritic regions and, in the as-produced condition, it appears mostly separated from the Sn-rich islands (center and bottom left in Fig. 2). Moreover, in all Si-containing alloys, minor intermetallic precipitates rich in Fe and Mn are present already in the as-produced state (center and bottom rows in Fig. 3). Optical microscopy (Fig. 2) and EDS elemental maps (Fig. 3) clearly show that, with increasing Si content, both the amount of Al–Si eutectic and the volumetric fraction of Fe- and Mn-containing intermetallics increase, in agreement with the concentrations of these elements reported in Table 1. In the as-produced condition, the Si-containing alloys exhibit porosity values of approximately 2 ± 1 $_{vol}$% and 3 ± 1 $_{vol}$% for Al-40Sn-3Si-Mg and Al-40Sn-4Si-Mg, respectively. These void levels are similar to that of the Si-free reference alloy (4 ± 1 $_{vol}$%).

After thermal cycling, the same phase constituents and main morphological features observed in the as-produced condition are substantially retained (central and bottom right in Fig. 2 and central and bottom rows in Fig. 4). In the Si-alloyed samples, coarsening of the Al dendritic matrix is significantly less pronounced than in the Al-40Sn reference alloy (right column in Fig. 2). Whereas in the cycled Si-free alloy, Sn reorganizes into pockets; in the Si-containing materials these regions appear associated with the Al-Si eutectic within the interdendritic areas, forming more compact and homogeneously distributed zones, as shown by the EDS maps in the central and bottom row of Fig. 4. The Fe-containing intermetallics remain clearly visible after thermal

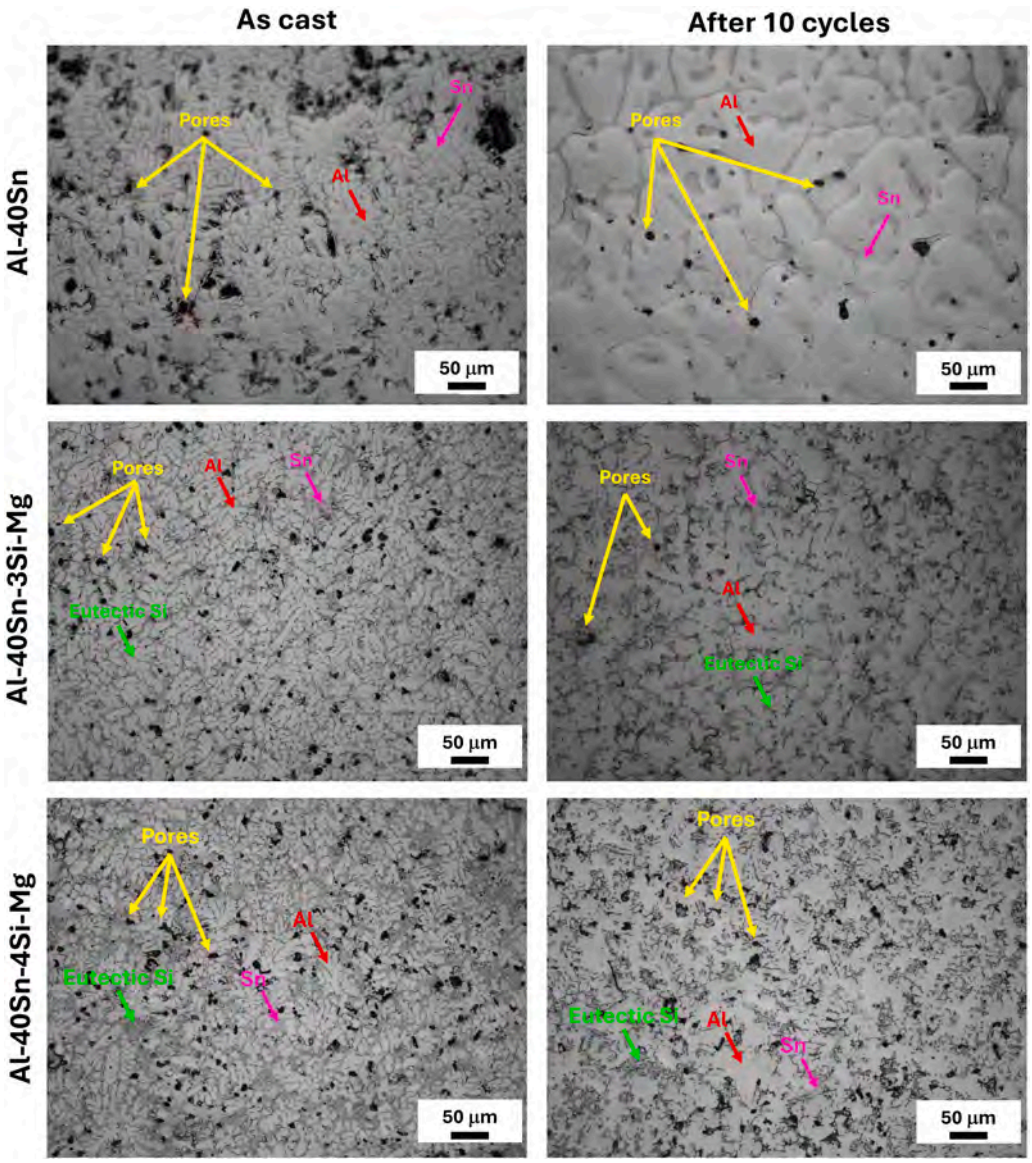

Fig. 2. Micrographs of the Al-40Sn, Al-40Sn-3Si-Mg and Al-40Sn-4Si-Mg ingot acquired at the core of the specimens. Micrographs on the left refer to as-produced specimens, while micrographs on the right to specimens which underwent 10 thermal cycles in the 25–270 °C temperature range.

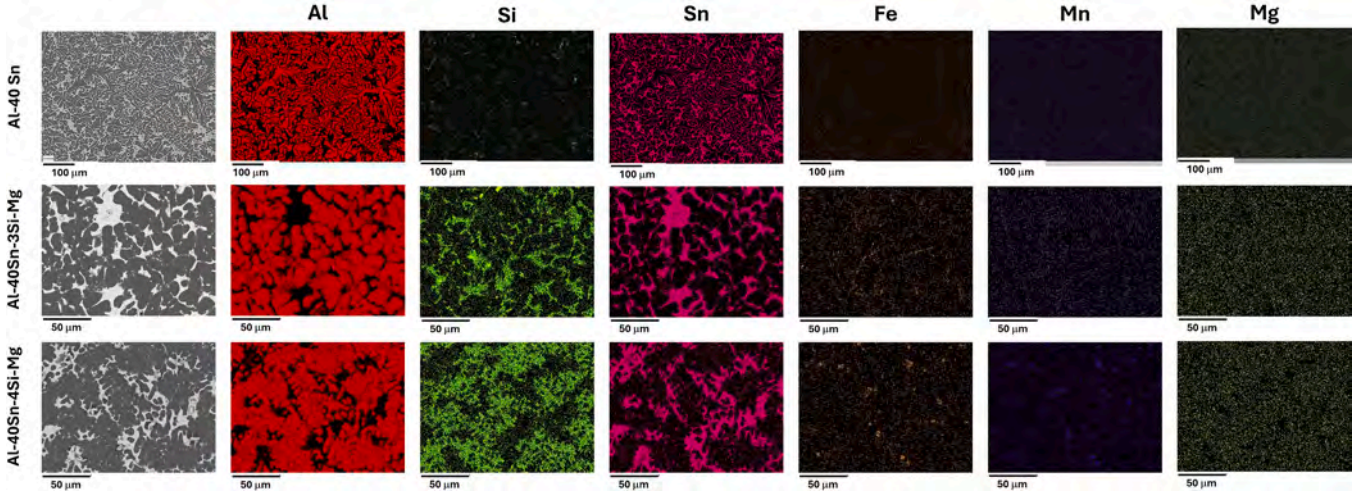

Fig. 3. EDS maps of the as produced Al-40Sn, Al-40Sn-3Si-Mg and Al-40Sn-4Si-Mg ingots acquired at the core of the metallographic samples.

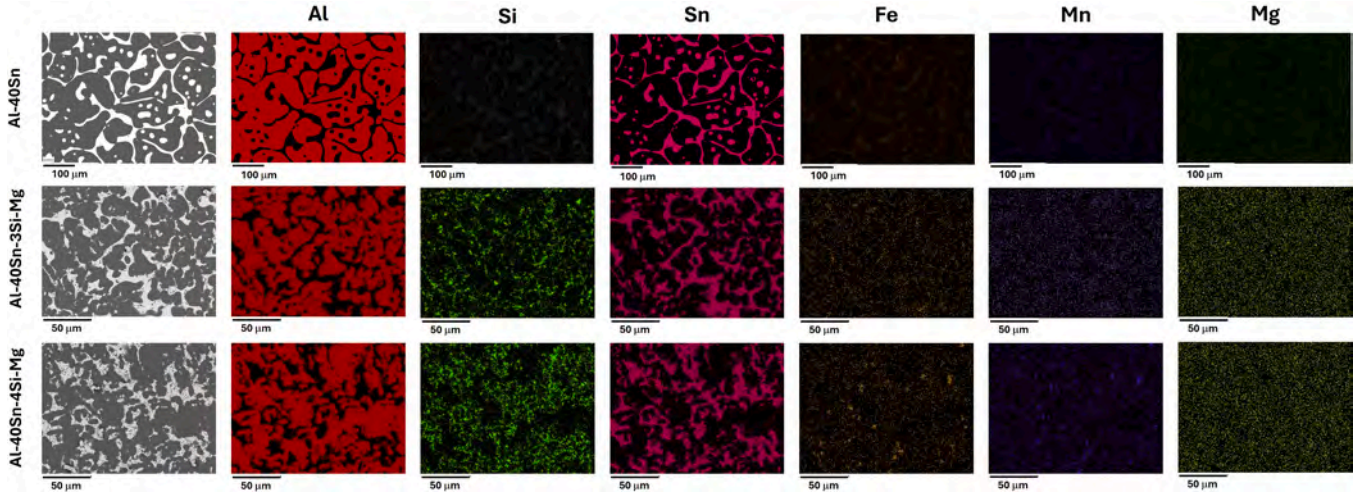

Fig. 4. EDS maps of the Al-40Sn, Al-40Sn-3Si-Mg and Al-40Sn-4Si-Mg ingots acquired at the core of the metallographic samples which underwent 10 thermal cycles in the 25–300 °C temperature range.

Table 2
Measured mass of the investigated samples before and after 10 thermal cycles, together with the corresponding mass variation.

	Initial mass [g]	Mass after 10 cycles [g]	Mass variation [%]
Al-40Sn	1.1649 ± 0.0001	1.1380 ± 0.0001	2.6
Al-40Sn-3Si-Mg	1.0319 ± 0.0001	1.0135 ± 0.0001	1.8
Al-40Sn-4Si-Mg	1.0114 ± 0.0001	0.9922 ± 0.0001	1.9

cycling and appear only slightly coarsened, without showing any evident interaction with the Sn-rich phase, in agreement with the EDS observations (central and bottom rows in Fig. 4). Importantly, the porosity level of the Si-alloyed samples remains substantially unchanged after thermal cycling, in contrast with the binary Al–Sn alloy, where porosity increases more markedly during repeated melting and solidification. In agreement with this microstructural observation, the mass variation measured before and after cycling (Table 2) is lower than that measured for the Si-free alloy, indicating a reduced tendency toward leakage of the Sn-rich liquid phase. The combination of stable porosity and limited mass loss therefore provides direct support for the improved cycling stability of the Si-containing alloys. This behavior is consistent with recent PCM studies suggesting that the Al–Si eutectic network acts as a restraining skeleton, limiting the migration of the low-melting Sn phase [32]. In line with other reports on Al–Si–Sn systems, Si promotes more effective dispersion and stabilization of the Sn-rich phase; e.g. micrographs of analogous plasma-sprayed alloys show that Sn remains well confined within the Al + Al-Si eutectic matrix even after multiple heating cycles [55]. Therefore, the enhanced stability of the Si-containing alloys after cycling can reasonably be attributed to the combined effects of a more stable interdendritic framework, improved confinement of the Sn-rich phase, and the resulting mitigation of leakage-related degradation. Compared with the binary Al-40Sn alloy, the Si-containing systems therefore exhibit a more stable microstructural response to cycling, characterized by reduced coarsening, lower leakage tendency, and essentially unchanged porosity.

The above microstructural observations are consistent with the phase assemblage predicted by equilibrium thermodynamic simulations. Equilibrium thermodynamic simulations at room temperature predict, for both the 3 and 4 $_{mass}$% Si alloys, the same set of phases expected from the combination of pure Sn (BCT_A5) and AlSiMg(Fe) casting alloys, i.e. primary Al (FCC_A1), Si (DIAMOND_A4) present here in form of Al–Si eutectic, α-Al(Mn,Fe)Si and $Al_9Fe_2Si_2$ intermetallics (AL15SI2M4 and AL9FE2SI2 respectively). In addition, Mg_2Sn-type intermetallic compounds (MG2SI_C1) are predicted in both Si-containing alloys. Their calculated amount is 0.38_{mass}% and 0.51_{mass}% for alloys containing 3 and 4_{mass}%Si, respectively. As the Si content and the concentration of minor alloying elements increase, the calculated mass fraction of all these secondary phases correspondingly increases (Figs. 5a and 5b). These predictions are in good agreement with the micrographs and EDS maps reported in Figs. 2 and 3, with the only exception of the Mg_2Sn-type intermetallic compound, which is not detectable at the magnifications employed but is nevertheless supported by literature evidence for similar alloy systems [32].

Thermodynamic simulations also provide the chemical composition of the phases in Al-40Sn-3Si-Mg and Al-40Sn-4Si-Mg, thereby allowing assessment of possible chemical interactions with the Sn introduced as PCM in the 20–300°C temperature range. At a fixed Sn content of 40_{mass}%, both experimental evidence and thermodynamic calculations indicate that the amount of secondary phases (Si, α-Al(Mn,Fe)Si, $Al_9Fe_2Si_2$ and Mg_2Sn) increases with increasing Si content, whereas their equilibrium chemical compositions remain essentially unchanged.

With the exception of Mg_2Sn, these secondary phases are predicted to contain negligible amounts of Sn. In particular, the Fe-containing intermetallics ($Al_9Fe_2Si_2$ and α-Al(Mn,Fe)Si) are predicted to consist solely of Al, Si, Fe and Mn, with no incorporation of Sn. This chemical independence from the Sn-rich phase is consistent with the EDS elemental maps reported in Fig. 3 (central and bottom rows). Similar Fe-based intermetallics have been previously reported in Al–Si–Sn alloy systems, where they are shown not to interfere with the Sn phase and, in some cases, to contribute to a more robust structural framework [56,57]. Thermo-Calc results further suggest that these Fe-containing intermetallics remain stable across the Sn solid–liquid transition, reinforcing their chemical and structural independence from the Sn-rich regions. In contrast, the Mg-bearing intermetallics predicted under equilibrium conditions (MG2SI_C1) display a chemical signature dominated by Mg and Sn, with Sn contents on the order of 70.61_{mass}% and only Si 0.14_{mass}% at room temperature. Based on its stoichiometry, it is therefore reasonable to infer that the main Mg-containing phase is Mg_2Sn.

3.2. Thermal analysis

Fig. 6 shows the DSC thermograms and the temperature-dependent specific heat capacity (C_p) curves in the 100–300 °C range, and the thermal diffusivity values obtained by LFA, for the Al-40Sn, Al-40Sn-3Si-

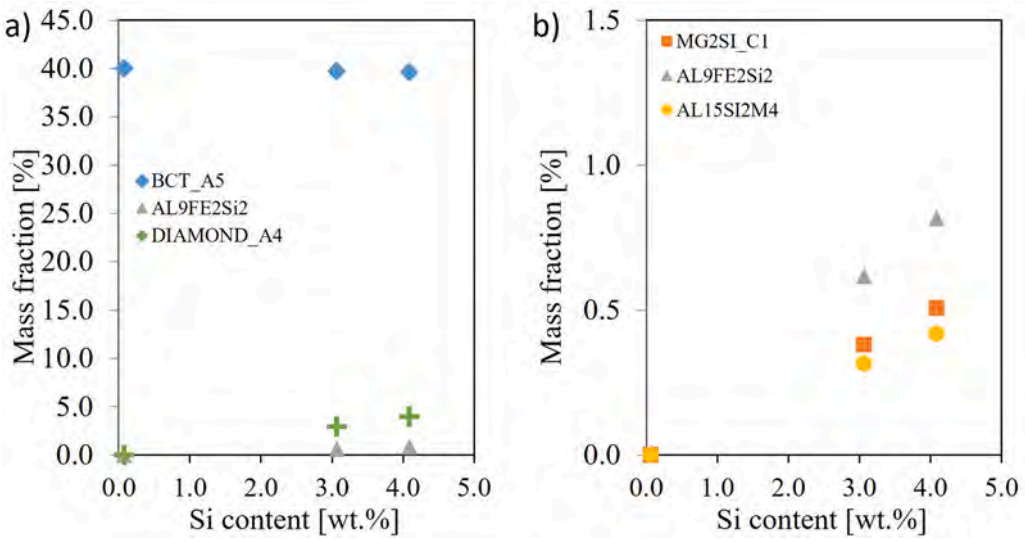

Fig. 5. Mass fraction of the phases predicted by thermodynamic simulations at room temperature for the investigated alloys having Si content ranging from 0 to 4_{mass}%: (a) overall phase assemblage; (b) magnified view of minor secondary phases, including Fe- and Mn-containing intermetallics and Mg_2Sn.

Mg, and Al-40Sn-4Si-Mg alloys in the investigated conditions. For each composition, data are shown both in the as-produced state and after 10 thermal cycles between 100 and 300 °C, enabling a direct assessment of how repeated heating influences their thermal behavior. The results of the thermodynamic simulations are also included for comparison (labelled as TC in the graphs).

3.2.1. *Al-40Sn alloy*

The binary Al-40Sn alloy provides a robust baseline for assessing the behavior of the multicomponent systems. As shown by the DSC curves in Fig. 6a and by the corresponding onset and offset transformation temperatures and enthalpies given in Figs. 7a and 7b, respectively, the DSC-derived values for the Al-40Sn alloy are in good agreement with the melting onset temperature and latent heat of fusion predicted by thermodynamic simulations, confirming the reliability of CALPHAD-based modelling of temperatures and enthalpic changes for this well-established system, in line with previous reports on binary and lightly alloyed Al–Sn PCMs [25]. The experimentally determined offset temperatures are systematically higher than those predicted under equilibrium conditions due to thermal lag and instrumental drift inherent to DSC measurements.

Regarding the specific heat capacity, the experimental measurements show a progressive decrease in C_p with increasing temperature, accompanied by a pronounced increment in the vicinity of the phase transition associated with Sn melting (Fig. 6b). At low temperatures (up to 130°C), the experimental values are in good agreement with thermodynamic predictions, suggesting that the intrinsic heat capacity of the alloy is correctly captured. The deviation observed at higher temperatures is therefore attributed to a combination of experimental and modelling-related factors. From an experimental standpoint, the use of alumina crucibles and finite heating rates may lead to a mismatch between the heat supplied to the crucible and the heat actually absorbed by the specimen, resulting in an apparent underestimation of C_p. On the modelling side, CALPHAD-based C_p values are derived under ideal equilibrium assumptions and do not account for kinetic effects associated with phase transformations and partial melting, which become increasingly relevant at elevated temperatures and may further contribute to the discrepancy between experimental and predicted C_p values.

Larger deviations between the experimental results and the outcome of the thermodynamic simulation are observed in the thermal diffusivity of the binary Al-Sn alloy, shown in Fig. 6c. As temperature increases, the thermal diffusivity exhibits an overall decreasing trend, which becomes markedly more pronounced in the vicinity of the Sn melting transition. At low temperatures, the measured values remain relatively stable and consistent with those expected for dense Al–Sn composites. Approaching the phase transition, however, the onset of Sn melting leads to a significant increase in data scatter and to anomalous diffusivity values. This behavior can be attributed to the progressive formation of a liquid Sn phase, which undergoes a pronounced reduction in thermal conductivity upon the solid–liquid transition [58]. This sharp decrease in the intrinsic heat-transport capability of Sn, combined with the presence of a liquid phase within the Al-rich matrix, promotes microstructural rearrangements, induces internal thermal discontinuities, and leads to a degradation of heat-transfer efficiency within the sample, thereby increasing signal dispersion.

After thermal cycling, both the DSC thermograms and the experimentally measured specific heat capacity curves closely reproduce the features observed during the first heating cycle (Figs. 6a, 6b and Figs. 7a and 7b). This behavior demonstrates that, despite the microstructural changes induced by cycling, the thermal response associated with the phase transition remains essentially unchanged, indicating that the fundamental thermodynamic characteristics of the Al–Sn eutectic are retained upon cycling. As expected, the specific heat capacity is not significantly affected by phase arrangement, but mainly depends on the nature and volume fraction of the constituent phases. By contrast, the thermal diffusivity measured by LFA is more sensitive to cycling. While the initial measurement aligns reasonably well with the values expected for dense Al–Sn composites, the experimentally determined diffusivity decreases significantly after repeated thermal cycling (Fig. 6c). This reduction can be attributed to several factors. First, the redistribution of Sn during the first cycle likely leads to its accumulation at the bottom surface of the sample, altering the effective thermal pathways and influencing the measured thermal properties. In addition, the reduction of thermal diffusivity can be associated with the increased porosity observed in the binary alloy after cycling across the activation temperature, resulting from Sn leakage during cycles performed outside the LFA. As widely reported in the literature [59,60], both the amount and morphology of porosity exert a strong influence on heat transport: increasing pore fractions reduce the effective thermal conductivity and, consequently, the thermal diffusivity, particularly when pores are interconnected or oriented transversally with respect to the heat flux direction. In addition to porosity development, other concurrent mechanisms may contribute to the observed diffusivity decrease of the

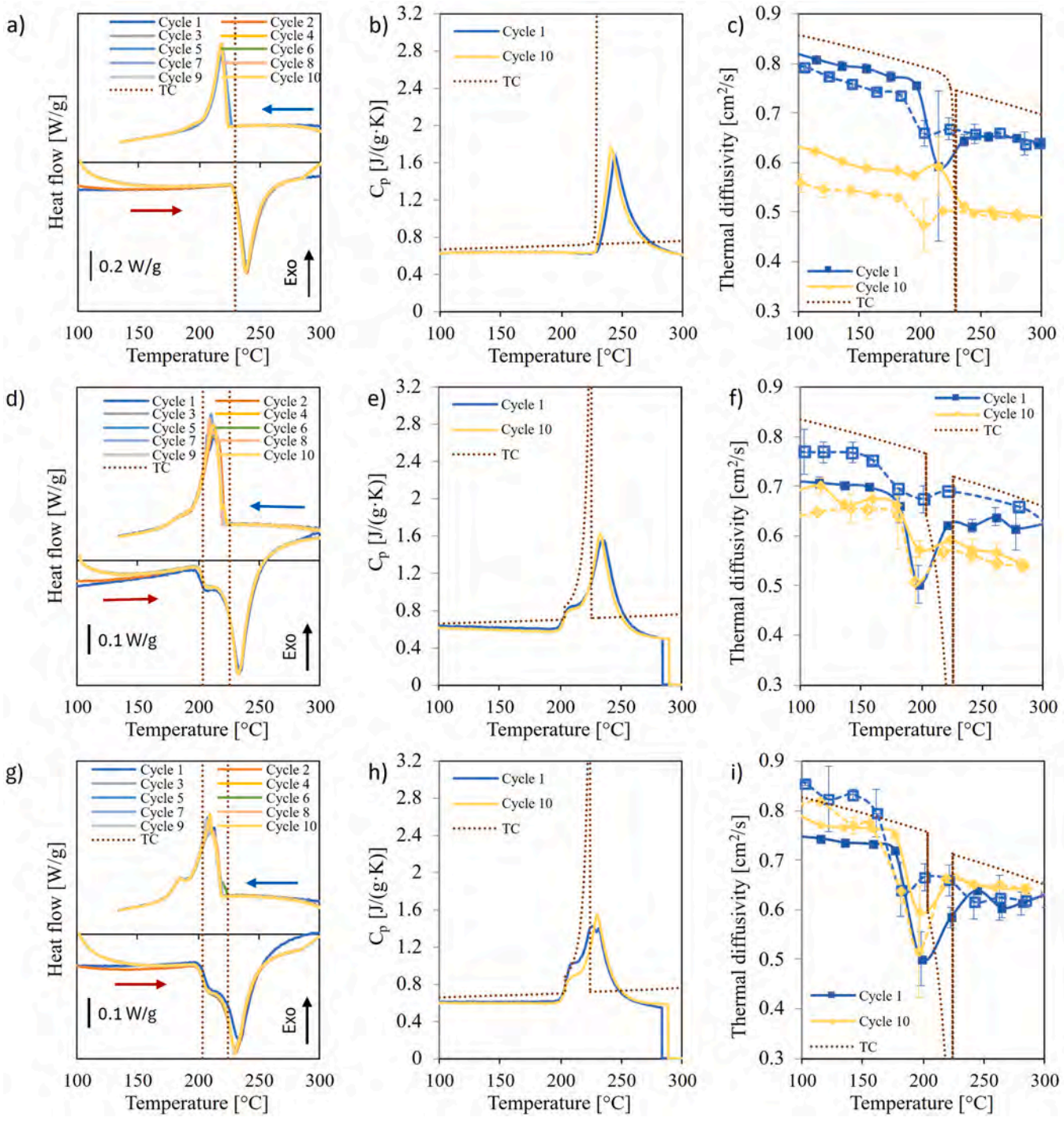

Fig. 6. DSC, specific heat capacity (C_p), and thermal diffusivity results for Al-40Sn, Al-40Sn-3Si-Mg and Al-40Sn-4Si-Mg alloys. Panels (a–c) refer to the Al-40Sn alloy, (d–f) to Al-40Sn-3Si-Mg and (g–i) to Al-40Sn-4Si-Mg. For all measurements, experimental data obtained during the 1st thermal cycle are shown in blue, while those from the 10th cycle are shown in yellow. In the LFA measurements, filled symbols correspond to heating ramps, whereas open symbols indicate cooling ramps. Thermodynamic simulation results obtained by Thermo-Calc are represented by the brown dotted lines in all plots. In the DSC graphs, the two vertical lines mark the simulated PCM activation temperature interval.

thermally cycled binary alloy. The formation of open porosity following Sn leakage can promote further oxidation of the internal surfaces, leading to the development of oxide layers within the pores that further hinder heat transfer. Moreover, thermal cycling induces substantial microstructural changes, as evidenced by the micrographs in the top row of Fig. 2, including dendritic coarsening of the Al-rich phase and redistribution of the Sn phase. Such microstructural rearrangements can disrupt continuous heat-conduction pathways within the metallic matrix, further reducing the effective thermal diffusivity of the alloy, which is a phase-arrangement dependent material property [44]. The same tendency is also reflected in the corresponding thermal conductivity values, calculated from thermal diffusivity, specific heat capacity, and density and reported in Table 3 together with those of the Si-containing alloys. In agreement with the diffusivity results, the binary Al-40Sn alloy shows a marked reduction in thermal conductivity after thermal cycling.

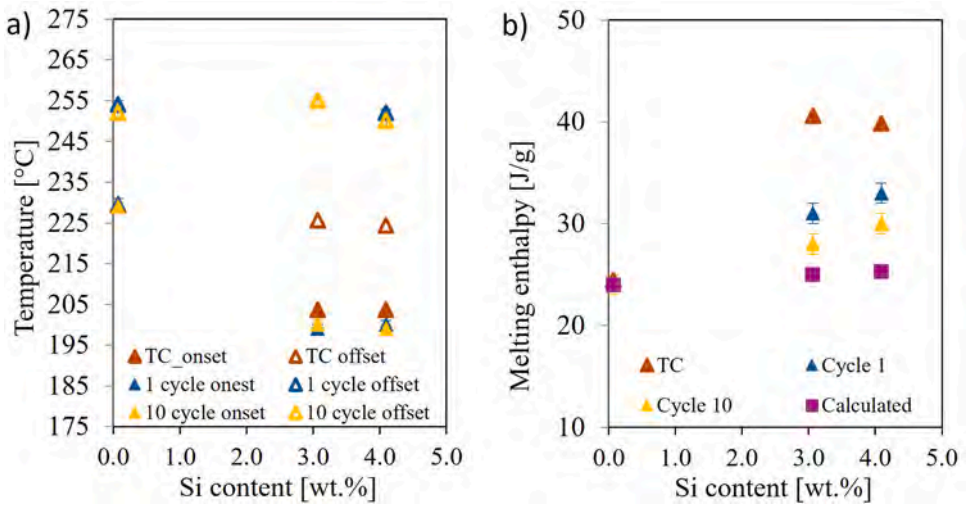

Fig. 7. (a) Onset and offset temperatures associated with the melting of the active phase as a function of Si content of the investigated alloys. (b) Enthalpy of fusion of the active phase as a function of Si content, as derived from DSC measurements. Experimental data at 1st cycle (blue) and 10th cycle (yellow) are compared to data derived from thermodynamic simulations (brown). The calculated enthalpy in (purple squares in panel b) was obtained indirectly by estimating the latent heat of transformation from the phase fractions predicted by thermodynamic simulations and the tabulated specific heats of Sn and the Mg_2Sn–Sn eutectic.

Table 3
Thermal conductivity values of the investigated alloys, calculated from thermal diffusivity, specific heat capacity, and density, at representative temperatures below and above the phase transition (175 and 260 °C), in the as-produced condition and after 10 thermal cycles.

Alloy	Condition	Thermal conductivity at 175 °C [W m^{-1} K^{-1}]	Thermal conductivity at 260 °C [W m^{-1} K^{-1}]
Al-40Sn	As-produced	144 ± 16	134 ± 18
	After 10 cycles	111 ± 12	107 ± 11
Al-40Sn-3Si-Mg	As-produced	143 ± 16	141 ± 14
	After 10 cycles	136 ± 14	115 ± 13
Al-40Sn-4Si-Mg	As-produced	149 ± 15	117 ± 12
	After 10 cycles	154 ± 16	140 ± 14

3.2.2. *Al-40Sn-3Si-Mg and Al-40Sn-4Si-Mg alloys*

When Sn is added to Al-based alloys containing Si, Mg, Mn and Fe as alloying elements, the endothermic peak associated with Sn melting undergoes a clear modification in shape, as shown by the DSC curves reported in Fig. 6d and Fig. 6g. In addition to the main melting peak of Sn, the DSC curves of the Al-40Sn-3Si-Mg alloy (Fig. 6d) and the Al-40Sn-4Si-Mg alloy (Fig. 6g) display a secondary endothermic signal of lower intensity appearing as a shoulder at temperatures below the onset of Sn melting. According to the thermodynamic equilibrium simulations and available literature data [61,62], this additional signal can be attributed to a eutectic melting event involving Mg_2Sn and Sn, which occurs close to 200°C. Although the corresponding eutectic constituent is too fine to be directly resolved at the magnifications employed in the present microstructural analysis, its occurrence is supported by the combined interpretation of DSC data, thermodynamic calculations, and literature evidence. This attribution is further supported by the Thermo-Calc evolution of phase mass percentages with temperature (Fig. 8), which shows that, within the same temperature interval, Mg_2Sn (MG2SI_C1) disappears, the amount of Sn (BCT_A5) decreases, and the percentage of liquid increases. Such a phase evolution is consistent with a eutectic melting event involving Mg_2Sn and Sn. The intensity of this eutectic-related signal increases systematically with increasing Mg (and Si) content, following the compositional sequence Al-40Sn-3Si-Mg < Al-40Sn-4Si-Mg (Fig. 6d and Fig. 6g, respectively) in agreement with the increasing fraction of Mg_2Sn predicted by the thermodynamic simulation (Fig. 4b).

The onset and offset values of the double-phase transition (including melting of both Mg_2Sn-Sn eutectic and Sn phase) for the alloys presented in Fig. 7a, show that they remain essentially constant for the Si-containing alloys. Similarly to what observed for the Al-40Sn alloy, the experimentally determined onset temperatures agree with those derived from the thermodynamic simulations, while the offset temperatures are consistently higher than the equilibrium predictions, reflecting the same thermal lag and instrumental drift effects observed for the offset values in the DSC measurements of the binary Al-Sn alloy.

The consistency in results with increasing Si content is also observed for the associated latent heats, with only minor variations that fall within the experimental uncertainty of the DSC measurements (Fig. 7b). Fig. 7b also includes the melting enthalpies obtained from thermodynamic simulations. A comparison between these and the experimentally determined melting enthalpies suggest that predictions tend to yield higher absolute values.

To gain further insight into the origin of this deviation, the individual enthalpic contributions associated with the different phases present in the alloys were examined in detail. The Fe-containing intermetallics, predicted by thermodynamic simulations (AL9FE2SI2 and AL15SI2M4) and confirmed by microstructural observations, can be excluded from the enthalpy balance, as they do not undergo any phase transformations within the investigated temperature range (100–300 °C). This is consistent with the absence of corresponding features in the DSC curves (Figs. 6d and 6g), confirming that these phases remain thermally inactive under the present conditions.

The dominant enthalpic contributions therefore arise from the melting of Sn (BCT_A5) and from the eutectic melting event involving Mg_2Sn (MG2SI_C1) and Sn. Based on the thermodynamic simulation results, the fraction of Mg_2Sn–Sn eutectic present in the alloys increases from 5.1% in the Al-40Sn-3Si-Mg alloy to 6.8% in the Al-40Sn-4Si-Mg alloy. Consequently, the corresponding fraction of Sn melting as pure Sn decreases from 34.9% (Al-40Sn-3Si-Mg) to 33.2% (Al- 40Sn-4Si-Mg) with increasing Si content.

To further assess the consistency between modelling and experiments, a phase-weighted theoretical latent heat was estimated by combining the phase fractions predicted in equilibrium at room temperature by thermodynamic simulations, with the melting enthalpies of the relevant transforming constituents (60 J/g for pure Sn, NIST SRM

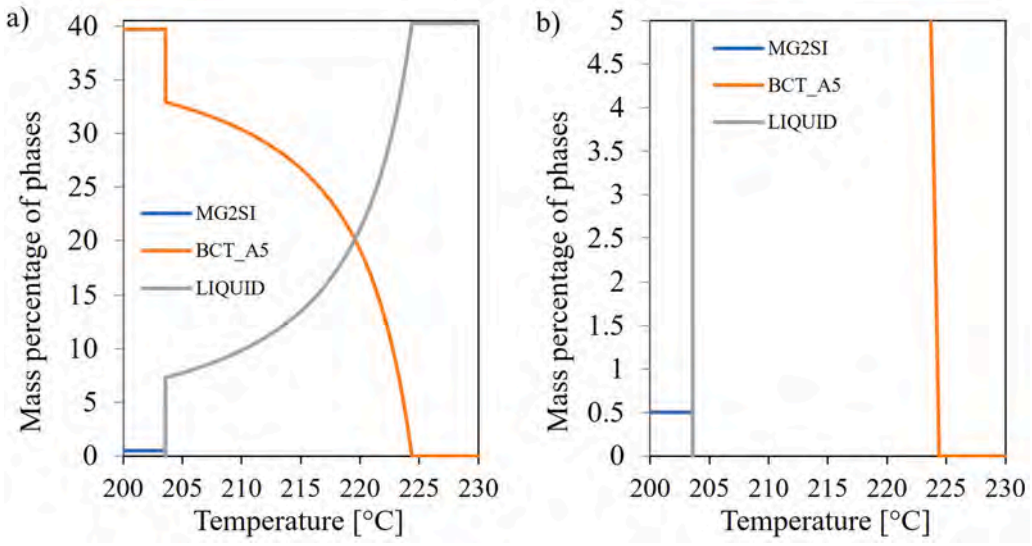

Fig. 8. Thermo-Calc-calculated variation of phase mass percentages as a function of temperature for the Al-40Sn-4Si-Mg alloy, shown here as a representative example: (a) overall evolution of Sn (BCT_A5), Mg_2Sn-type phase (MG2SI), and liquid fraction in the 200–230 °C range; (b) magnified view highlighting the low fraction of the Mg_2Sn-type phase and its disappearance in correspondence with the onset of liquid formation.

2220, and 68 J/g for the Mg_2Sn–Sn eutectic, [62]). The fraction of the Mg_2Sn –Sn eutectic was derived from the Mg-Sn binary phase diagram and from the amount of Mg_2Sn predicted by CALPHAD. By applying the lever rule at the eutectic composition, the relative amounts of Sn and Mg_2Sn within the eutectic were estimated to be about 93 $_{mass}$% and 7 $_{mass}$%, respectively. The remaining Sn fraction according to CALPHAD predictions was then taken as the amount of pure Sn available for melting outside the eutectic constituent. Accordingly, the theoretical latent heat was calculated as the linear combination of the contributions associated with pure Sn melting and Mg_2Sn–Sn eutectic melting. In this approach, the eutectic was treated as a distinct phase-change domain, whose specific enthalpy was taken as the enthalpy jump associated with melting of an alloy with eutectic composition. Therefore, the calculation should be regarded as a first-order approximation of the eutectic contribution to the overall latent heat. The resulting phase-weighted latent heat values are reported in Fig. 7b, while the corresponding phase fractions and partial enthalpic contributions are summarized in Table 4.

The calculated fusion enthalpies underestimate the experimentally measured values. This discrepancy is plausibly related to the fact that, in addition to the melting of these two phases, other thermally activated processes may occur within the alloy and contribute to the overall thermal response, thereby altering the measured heat flow. Nevertheless, the trend obtained by considering only the latent heat contributions of the Sn-rich phases is significantly closer to the experimental results than the direct outputs of the thermodynamic simulations, indicating that the phase-weighted approach captures the dominant contributions to the melting enthalpy more effectively. The differences between the direct outputs of the thermodynamic simulations and the experimental data in the determination of the latent heat of fusion for the Al-40Sn-3Si-Mg and Al-40Sn-4Si-Mg alloys may reflect the intrinsic challenges associated with describing complex multicomponent eutectic reactions under equilibrium assumptions, particularly in proximity to phase transitions where numerical sensitivity and database uncertainties can play a role.

The specific heat capacity (C_p) measured for the Si-containing alloys (Figs. 6e and 6h) shows a comparatively limited sensitivity to alloy composition, similarly to what observed for the transition temperature interval and for the latent heat. While the baseline C_p values are only weakly affected by composition, marked differences emerge in the magnitude and temperature span of the C_p variation associated with phase transitions. In particular, the intensity of the C_p increment during melting progressively decreases as the Si content, and concurrently the Mg content, increases, whereas the temperature interval over which this variation occurs becomes broader.

This trend reflects the transition from a sharp and intense C_p peak in the binary alloy, associated with the melting of essentially pure Sn, to a more distributed thermal response in the multicomponent systems, where melting involves both pure Sn and the Mg_2Sn–Sn eutectic. As a consequence, in the multicomponent alloys the phase-change-related C_p enhancement is spread over a wider temperature range but with reduced peak intensity, while in the binary alloy it appears more localized and pronounced.

Thermodynamic equilibrium simulations, reported as brown dotted curves in Figs. 6e and 6h, are consistent with these experimental observations, predicting an almost composition-independent C_p with only a slight decrease when moving from the binary alloy to the multicomponent systems and no significant variation with increasing Si (and Mg) alloying element content. This agreement supports the interpretation that the sensible heat contribution is largely governed by Al and Sn, whose high volume fractions dominate the overall C_p response, while the contributions of secondary phases remain comparatively minor.

Table 4
Phase fractions and partial enthalpy contributions used for the calculation of the theoretical latent heat of the investigated alloys.

Alloy	Mg_2Sn–Sn eutectic fraction [mass%]	Enthalpic Contribution of Mg_2Sn–Sn eutectic [J/g]	Pure Sn fraction [mass%]	Enthalpic Contribution of pure Sn [J/g]	Calculated latent heat [J/g]
Al-40Sn	-	-	40	24	24
Al-40Sn-3Si-Mg	5.1	4	34.9	21	25
Al-40Sn-4Si-Mg	6.8	5	33.2	20	25

Focusing the attention on the temperature-dependence of C_p, thermodynamic equilibrium simulations predict a slight increase in specific heat with increasing temperature. Experimentally, however, a weak but systematic decrease in C_p is observed as temperature increases. This discrepancy mirrors the behavior already discussed for the binary alloy.

Although porosity does not directly affect the gravimetric C_p values (expressed in J/(g•K)), it may nonetheless have a detrimental impact on the sensible heat storage capability of the material in thermal energy storage applications, as it reduces the effective volumetric heat capacity.

With regard to thermal diffusivity (Figs. 6f and 6i), the experimental measurements reveal a clear decrease with increasing temperature, with a pronounced drop in the vicinity of the melting of the active phase, consistent with the onset of partial melting and the associated reduction in effective heat-transport pathways. This behavior closely mirrors that previously observed for the binary alloy (Fig. 6c), the main difference being that the diffusivity drop occurs at lower temperatures, in agreement with the earlier onset of melting associated with the Mg_2Sn–Sn eutectic. Predictions obtained from the thermodynamic simulations (brown dotted curves in Fig. 6c, Fig. 6f and Fig. 6i) show good agreement with this experimentally observed trend. The thermal diffusivity behavior of the Si-containing alloys can be interpreted in relation to their more stable microstructure after cycling. In these materials, the limited porosity evolution, the lower mass loss measured after cycling (Table 2), and the more compact distribution of the Sn-rich phase within the interdendritic Al-Si eutectic regions help preserve the continuity of the heat-transfer paths. This explains why, although the absolute thermal diffusivity is slightly lower than that of the binary Al-40Sn alloy, its evolution upon cycling remains substantially more stable in the Si-containing systems.

To complement the transient heat-transfer analysis based on thermal diffusivity, the corresponding thermal conductivity values were also estimated from the experimental thermal diffusivity, specific heat capacity, and density, according to $k = \alpha \rho C_p$. Since the aim is to provide a concise comparison rather than a full temperature-resolved conductivity analysis, representative values below and above the phase transition are reported in Table 3, at 175 and 260 °C, respectively. The values at 260 °C should be regarded as representative estimates of the high-temperature condition, since in some cases the C_p contribution associated with the phase transition had not yet fully returned to the baseline at this temperature. At the same time, the use of higher temperatures would have reduced the available margin to the end of the DSC run, which is not ideal for a rigorous C_p determination. The calculated thermal conductivity values therefore show some composition- and condition-dependent scatter across the phase-transition interval. Nevertheless, they still allow a meaningful comparative assessment: while the binary Al-40Sn alloy exhibits a marked reduction in thermal conductivity after thermal cycling, the Si-containing alloys retain more stable values, in agreement with their reduced porosity evolution and improved confinement of the Sn-rich phase within the interdendritic microstructure.

Notably, all these results are largely preserved even after 10 thermal cycles between 100 and 300 °C. In particular, despite the microstructural rearrangements induced by cycling, the DSC response associated with the phase-change events, i.e. the onset of melting, the latent heat, and the specific heat capacity, remains essentially unchanged, as evidenced by the curves in Fig. 6d, Fig. 6e, Fig. 6g and Fig. 6h. Compared with the binary Al-40Sn alloy, the multicomponent systems exhibit a more stable heat-transfer response upon thermal cycling, reflecting their enhanced microstructural stability. Although the absolute thermal diffusivity and thermal conductivity values show some composition- and condition-dependent variations, the Si-containing alloys retain their heat-transfer properties more effectively after cycling, which largely offsets any reduction observed under specific conditions.

From an application perspective, this is a critical advantage: a phase change material whose thermal diffusivity remains stable during repeated melting–solidification cycles ensures predictable and reproducible heat charging and discharging rates, thereby preserving thermal efficiency and reliability over long-term operation. Consequently, the improved resistance to microstructural degradation in the Al-40Sn-3Si-Mg and Al-40Sn-4Si-Mg alloys outweighs the modest reduction in absolute diffusivity, making these alloys more suitable for practical PCM applications where durability and consistent thermal performance are essential. Overall, these results indicate that the fundamental thermodynamic behavior of the Sn-based phase-change reactions is retained upon cycling, while cycling primarily affects the heat transport capability rather than the intrinsic thermal response of the material.

Finally, it is worth noting that the presence of porosity, while detrimental in terms of volumetric latent heat, effective specific heat capacity, and thermal diffusivity, may also play a beneficial mechanical role. In particular, the development of controlled porosity can partially accommodate the volumetric expansion associated with Sn melting, thereby reducing the internal stresses generated during repeated phase-change cycles [63]. The mitigation of these thermally induced stresses limits damage accumulation within the material, such as crack initiation or interfacial decohesion, and can ultimately contribute to extending the service lifetime of the PCM component. From this perspective, a moderate reduction in thermal performance due to porosity may represent an acceptable trade-off when balanced against improved mechanical compliance and enhanced durability under long-term thermal cycling.

4. Conclusions

This study investigated the effect of Si content on the thermal response, microstructural stability, and cycling behavior of composite metallic phase change materials based on Al-Si-Sn system containing a fixed 40_{mass}% Sn fraction. By integrating experimental thermal analysis, microstructural characterization, and CALPHAD-based thermodynamic modelling, the interplay between composition, secondary phases, porosity, and thermophysical performance was systematically assessed.

The results demonstrate that varying the Si content of the investigated alloys in the range 0–4_{mass}%, with concurrent minor changes in Mg content in Si-bearing alloys does not significantly affect the melting temperature nor the latent heat associated with the active phase melting. This confirms that the primary phase-change functionality is preserved across all investigated alloys. However, the variations in chemical composition strongly influences the temperature span of the thermal transition due to the concurrent melting of a secondary eutectic, i.e. Mg_2Sn-Sn, which lead to a more distributed and smoother phase-change behavior compared to the binary Al–Sn reference system.

From a microstructural standpoint, the addition of Si substantially improves stability under repeated thermal cycling. The Al–Si eutectic network promotes a more homogeneous and constrained distribution of the Sn-rich phase and effectively limits porosity evolution. As a result, the thermal response associated with the phase change remains highly reproducible after cycling, and the thermal diffusivity shows significantly enhanced stability, despite a small reduction in its absolute value relative to the binary alloy.

Porosity was found to have a dual effect: while it reduces the effective volumetric latent heat, specific heat capacity, and thermal diffusivity, it also contributes beneficially by accommodating the volumetric expansion of Sn during melting, thereby mitigating thermally induced stresses and improving long-term durability.

Overall, the findings identify Si as a key design parameter for balancing thermal performance and cycling stability in Al–Sn-based metallic PCMs. The improved structural robustness and reproducible thermal behavior make Al–Si–Sn alloys promising candidates for medium-temperature thermal energy storage applications where durability and consistent performance are essential.

CRediT authorship contribution statement

Marola Silvia: Writing – original draft, Visualization, Validation, Methodology, Investigation, Formal analysis. **Matteo Molteni:** Writing – review & editing, Visualization, Methodology, Investigation, Formal analysis. **Paola Bassani:** Writing – review & editing, Funding acquisition. **Elisabetta Gariboldi:** Writing – review & editing, Supervision, Project administration, Funding acquisition.

Declaration of Competing Interest

The authors declare the following financial interests/personal relationships which may be considered as potential competing interests: Elisabetta Gariboldi and Paola Bassani reports financial support was provided by European Innovation Council and SMEs Executive Agency. Given her role as editor, Elisabetta Gariboldi had no involvement in the peer review of this article and had no access to information regarding its peer review. Full responsibility for the editorial process for this article was delegated to another journal editor. If there are other authors, they declare that they have no known competing financial interests or personal relationships that could have appeared to influence the work reported in this paper.

Acknowledgements

The research has been carried out within the M-TES “Metallic phase change material-composites for Thermal Energy management” project (grant number 101115307) funded by the European Union. Views and opinions expressed are however those of the author(s) only and do not necessarily reflect those of the European Union or EISMEA – European Innovation Council and SMEs Executive Agency. Neither the European Union nor the granting authority can be held responsible for them. The author acknowledge for the support.

Appendix A. Supporting information

Supplementary data associated with this article can be found in the online version at doi:10.1016/j.jallcom.2026.188288.

References

[1] J.Z. Zhao, T. Ahmed, H.X. Jiang, J. He, Q. Sun, Solidification of immiscible alloys: a review, Acta Metall. Sin. (Engl. Lett.) 30 (2017) 1–28, https://doi.org/10.1007/s40195-016-0523-x.
[2] Q. Liu, N. Luo, Z. Fu, B. Niu, X. Wu, X. Wang, D. Mei, Q. Li, B. Song, J. He, Additive manufacturing of immiscible alloys: breaking the preparation bottleneck and unlocking the property potential, J. Alloy. Compd. 1027 (2025), https://doi.org/10.1016/j.jallcom.2025.180544.
[3] C. Deng, T. Xie, Z. Wan, G. Feng, Y. Yang, Z. Wu, X. Wang, S. Zhou, J. Chen, Microstructure and properties of cu-fe immiscible coatings fabricated via combined mechanical alloying and laser cladding, Materials 18 (2025), https://doi.org/10.3390/ma18194436.
[4] C. Wei, J. Wang, Y. He, J. Li, E. Beaugnon, Solidification of immiscible alloys under high magnetic field: A review, Met. (Basel) 11 (2021) 1–21, https://doi.org/10.3390/met11030525.
[5] O.S. Roik, O.M. Yakovenko, V.P. Kazimirov, V.E. Sokol’skii, N.V. Golovataya, Y. O. Kashirina, Structure of liquid Al-Sn alloys, J. Mol. Liq. 330 (2021), https://doi.org/10.1016/j.molliq.2021.115570.
[6] Y. Li, H. Jiang, H. Sun, L. Zhang, J. He, J. Zhao, Microstructure evolution of immiscible alloy solidified under the effect of composite electric and magnetic fields, J. Mater. Sci. Technol. 162 (2023) 247–259, https://doi.org/10.1016/j.jmst.2023.04.018.
[7] Y. Wen, X. Wu, A. Huang, R.L. Narayan, P. Wang, L. Zhang, B. Zhang, U. Ramamurty, X. Qu, Laser powder bed fusion of immiscible steel and bronze: a compositional gradient approach for optimum constituent combination, Acta Mater. 264 (2024), https://doi.org/10.1016/j.actamat.2023.119572.
[8] R.P. Minneci, E.A. Lass, J.R. Bunn, H. Choo, C.J. Rawn, Copper-based alloys for structural high-heat-flux applications: a review of development, properties, and performance of Cu-rich Cu–Cr–Nb alloys, Int. Mater. Rev. 66 (2021) 394–425, https://doi.org/10.1080/09506608.2020.1821485.
[9] H.T. Hai, H. Takamura, J. Koike, Oxidation behavior of Cu-Ag core-shell particles for solar cell applications, J. Alloy. Compd. 564 (2013) 71–77, https://doi.org/10.1016/j.jallcom.2013.02.048.
[10] H. Zhu, I. Turkevych, H. Lohan, P. Liu, R.W. Martin, F.C.P. Massabuau, R.L. Z. Hoye, Progress and applications of (Cu–)Ag–Bi–I semiconductors, and their derivatives, as next-generation lead-free materials for photovoltaics, detectors and memristors, Int. Mater. Rev. 69 (2024) 19–62, https://doi.org/10.1177/09506608231213065.
[11] J. Daimari, S. Basumatary, A.K. Deka, Bimetallic nanoparticles from coinage metals (Cu, Ag, Au) and its biomedical applications: A Review, Nano-Struct. Nano-Objects 39 (2024), https://doi.org/10.1016/j.nanoso.2024.101247.
[12] H. Zhang, T. Liu, S. Zhao, Z. Xu, Y. Lv, J. Fan, Y. Han, Size-dependent alloying ability of immiscible w-cu bimetallic nanoparticles: a theoretical and experimental study, Nanomaterials 11 (2021) 1–7, https://doi.org/10.3390/nano11041047.
[13] B.K.D. Barman, S.P. Singh, P. Kumar, Processing and mechanical behavior of Cu-Bi alloys with high volume fraction of Bi: suitability for high temperature soldering application, Materials Science Engineering A 666 (2016) 339–349, https://doi.org/10.1016/j.msea.2016.04.068.
[14] Y. Liu, G. Shao, P. Tsakiropoulos, Thermodynamic reassessment of the Mo±Si and Al±Mo±Si systems, Intermet. (Barking) 8 (2000) 953–962.
[15] L. Chang, K. Li, Z. Cai, P. Du, Y. Wang, C. Zhou, E. Jiao, A.R. Khan, G. Xie, W. Bao, H. Zhang, Synergistic mechanical-degradation coupling in novel immiscible Mo–Cu alloy for biodegradable implant applications, J. Mater. Res. Technol. 39 (2025) 6081–6095, https://doi.org/10.1016/j.jmrt.2025.10.207.
[16] K. Hyun Kim, M. Slazhniev, S. Won Kim, H. Suk Sim, K. Euh, Study on controlled segregation of Al-Sn alloys for bearings, in: 8th International Conference on Electromagnetic Processing of Materials, Cannes, France, 2015. ⟨https://hal.science/hal-01334926v1⟩.
[17] M. Zhu, Y. Gao, C.Y. Chung, Z.X. Che, K.C. Luo, B.L. Li, Improvement of the wear behaviour of Al-Pb alloys by mechanical alloying, Wear 242 (2000) 47–53.
[18] A. Inoue, N. Yano, K. Matsuzaki, T. Masumoto, Microstructure and superconducting properties of melt-quenched insoluble AI-Pb and AI-Pb-Bi alloys, J. Mater. Sci. 22 (1987) 123–131.
[19] P.L. Schaffer, R.H. Mathiesen, L. Arnberg, M. Di Sabatino, A. Snigirev, situ investigation of spinodal decomposition in hypermonotectic Al-Bi and Al-Bi-Zn alloys, N. J. Phys. 10 (2008), https://doi.org/10.1088/1367-2630/10/5/053001.
[20] J.X. Zhang, M.J. Zhang, H.F. Li, H.Z. Gu, D. Chen, C.H. Zhang, Y.F. Tian, E.J. Wang, Q.N. Mu, Near zero thermal performance loss of Al-Si microcapsules with fibers network embedded Al2O3/AlN shell, J. Mater. Sci. Technol. 176 (2024) 48–56, https://doi.org/10.1016/j.jmst.2023.07.060.
[21] J. Zhang, M. Zhang, H. Gu, C.R. Bowen, H. Li, A. Huang, L. Fu, X. Liu, Processing and properties of Al-Si microcapsules with a biomimetic-corrugated structure and corundum-mullite composite shell, J. Mater. 11 (2025), https://doi.org/10.1016/j.jmat.2024.06.003.
[22] M. Molteni, E. Gariboldi, Review on the role of metals in the field of phase change materials: From their use for thermal energy storage to multifunctional applications, Int. J. Heat. Mass Transf. 256 (2026), https://doi.org/10.1016/j.ijheatmasstransfer.2025.128078.
[23] A.J. Mcalister, D.J. Kahan, The Al-Sn (Aluminum-Tin) System, Bull. Alloy Phase Diagr. 4 (1983) 410–414.
[24] H. Sugo, E. Kisi, D. Cuskelly, Miscibility gap alloys with inverse microstructures and high thermal conductivity for high energy density thermal storage applications, Appl. Therm. Eng. 51 (2013) 1345–1350, https://doi.org/10.1016/j.applthermaleng.2012.11.029.
[25] D. Manasijević, L. Balanović, I. Marković, M. Gorgievski, U. Stamenković, A. Kovačević, Thermal properties and microstructure of Al–Sn alloys, J. Phys. Chem. Solids 195 (2024), https://doi.org/10.1016/j.jpcs.2024.112297.
[26] P.J. Shamberger, N.M. Bruno, Review of metallic phase change materials for high heat flux transient thermal management applications, Appl. Energy 258 (2020), https://doi.org/10.1016/j.apenergy.2019.113955.
[27] R.A. Kishore, S. Priya, Low-grade waste heat recovery using the reverse magnetocaloric effect, Sustain. Energy Fuels 1 (2017) 1899–1908, https://doi.org/10.1039/c7se00182g.
[28] J.Paulus Kotzé, Thermal energy storage in metallic phase change materials, Stellenbosch University, 2014. ⟨http://scholar.sun.ac.za⟩.
[29] A.I. Fernández, C. Barreneche, M. Belusko, M. Segarra, F. Bruno, L.F. Cabeza, Considerations for the use of metal alloys as phase change materials for high temperature applications, Sol. Energy Mater. Sol. Cells 171 (2017) 275–281, https://doi.org/10.1016/j.solmat.2017.06.054.
[30] N.A. Belov, A.O. Mikhailina, A.N. Alabin, O.O. Stolyarova, Theoretical and experimental study of the Al – Cu – Si – Sn phase diagram in the range of aluminum alloys, Met. Sci. Heat. Treat. 58 (2016) 195–201, https://doi.org/10.1007/s11041-016-9988-5.
[31] F. Bertelli, E.S. Freitas, N. Cheung, M.A. Arenas, A. Conde, J. de Damborenea, A. Garcia, Microstructure, tensile properties and wear resistance correlations on directionally solidified Al-Sn-(Cu; Si) alloys, J. Alloy. Compd. 695 (2017) 3621–3631, https://doi.org/10.1016/j.jallcom.2016.11.399.
[32] P. Bassani, M. Molteni, E. Gariboldi, Microstructural features and thermal response of granulated Al and A356 alloy with relevant Sn additions, Mater. Des. 229 (2023), https://doi.org/10.1016/j.matdes.2023.111879.
[33] C. Confalonieri, M. Perrin, E. Gariboldi, Combined powder metallurgy routes to improve thermal and mechanical response of Al−Sn composite phase change materials, Trans. Nonferrous Met. Soc. China (Engl. Ed.) 30 (2020) 3226–3239, https://doi.org/10.1016/S1003-6326(20)65456-5.
[34] H.X. Jiang, J.Z. Zhao, Solidification of immiscible alloys under the effect of electric and magnetic fields, Acta Metall. Sin. (Engl. Lett.) 31 (2018) 1240–1248, https://doi.org/10.1007/s40195-018-0731-7.

[35] W. Zhai, B.J. Wang, H.M. Liu, L. Hu, B. Wei, Three orthogonal ultrasounds fabricate uniform ternary Al-Sn-Cu immiscible alloy, Sci. Rep. 6 (2016), https://doi.org/10.1038/srep36718.
[36] S. Li, Y. Li, H. Guo, Z. Wen, Z. Zhu, Effect of electromagnetic stirring frequency on tribological performance and corrosion resistance of Al-Sn bearing alloy, Mater. Today Commun. 32 (2022), https://doi.org/10.1016/j.mtcomm.2022.103898.
[37] C. Confalonieri, A.T. Grimaldi, E. Gariboldi, Ball-milled Al–Sn alloy as composite Phase Change Material, Mater. Today Energy 17 (2020), https://doi.org/10.1016/j.mtener.2020.100456.
[38] C. Confalonieri, R. Casati, E. Gariboldi, Effect of process parameters on laser powder bed fusion of Al-Sn miscibility gap alloy, Quantum Beam Sci. 6 (2022) 1–15, https://doi.org/10.3390/qubs6020017.
[39] K.S. Cruz, E.S. Meza, F.A.P. Fernandes, J.M.V. Quaresma, L.C. Casteletti, A. Garcia, Dendritic arm spacing affecting mechanical properties and wear behavior of Al-Sn and Al-Si alloys directionally solidified under unsteady-state conditions, Metall. Mater. Trans. A Phys. Metall. Mater. Sci. 41 (2010) 972–984, https://doi.org/10.1007/s11661-009-0161-2.
[40] T. El-Ashram, Amorphous and metastable crystalline structures in rapidly solidified Sn-Al system using melt-spinning technique, Radiat. Eff. Defects Solids 159 (2004) 535–538, https://doi.org/10.1080/10420150412331323041.
[41] T. Marrocco, L.C. Driver, S.J. Harris, D.G. McCartney, Microstructure and properties of thermally sprayed al-sn-based alloys for plain bearing applications, Proc. Int. Therm. Spray. Conf. (2006) 634–639, https://doi.org/10.1361/105996306X147009.
[42] X.J. Ning, J.H. Kim, H.J. Kim, C. Lee, Characteristics and heat treatment of cold-sprayed Al-Sn binary alloy coatings, Appl. Surf. Sci. 255 (2009) 3933–3939, https://doi.org/10.1016/j.apsusc.2008.10.074.
[43] P.J. Shamberger, Cooling capacity figure of merit for phase change materials, J. Heat. Transf. 138 (2016) 1–8, https://doi.org/10.1115/1.4031252.
[44] M. Molteni, I.M. Carraretto, P. Bassani, E. Gariboldi, A. Lucchini, L.P.M. Colombo, Critical assessment of thermal conductivity models for Miscibility Gap Alloy-based composite Phase Change Materials for high temperature Thermal Energy Storage, n.d.
[45] C.A. Kang, Y.H. Lee, H. Park, J.M. Park, T. Zhanfeng, J.S. Roh, S. rak Park, Y. H. Cho, J.I. Lee, Y.H. Jo, Correlation between microstructure, tensile properties, and thermal conductivity of non-heat-treated Al-Si casting alloys fabricated by high-pressure die-casting, J. Mater. Res. Technol. 39 (2025) 9848–9860, https://doi.org/10.1016/j.jmrt.2025.11.213.
[46] J.K. Chen, H.Y. Hung, C.F. Wang, N.K. Tang, Effects of casting and heat treatment processes on the thermal conductivity of an Al-Si-Cu-Fe-Zn alloy, Int. J. Heat. Mass Transf. 105 (2017) 189–195, https://doi.org/10.1016/j.ijheatmasstransfer.2016.09.090.
[47] J.M. Molina, A. Rodríguez-Guerrero, E. Louis, F. Rodríguez-Reinoso, J. Narciso, Porosity effect on thermal properties of Al-12 wt% Si/graphite composites, Materials 10 (2017), https://doi.org/10.3390/ma10020177.
[48] K. Pietrak, T.S.W. Wiśniewski, A review of models for effective thermal conductivity of composite materials, J. Power Technol. 95 (2015) 14–24.
[49] M. Molteni, A.M. Grande, P. Bassani, E. Gariboldi, Role of microstructure in the exploitation of self-healing potential in form-stable composite phase change materials based on immiscible alloys, J. Alloy. Compd. 984 (2024), https://doi.org/10.1016/j.jallcom.2024.173989.
[50] O.J. Van Der Schijff, N. Budiansky, R.M. Latanision, Liquid-Metal- and Solid-Metal-Induced Embrittlement. in: Failure Analysis and Prevention, ASM International, 2021, pp. 573–580, https://doi.org/10.31399/asm.hb.v11.a0006786.
[51] V. Alcántara Alza, Spheroidizing in steels: processes, mechanisms, kinetic and microstructure-a review, IOSR J. Mech. Civ. Eng. (IOSR-JMCE) 18 (2021) 63–81.
[52] C. Confalonieri, E. Boller, Y. Cheng, E. Gariboldi, Synchrotron radiation micro-CT with phase contrast for high-temperature in-situ microstructural characterization of Al[sbnd]Sn composite phase change materials, Mater. Charact. 193 (2022), https://doi.org/10.1016/j.matchar.2022.112302.
[53] P. Nikolopoulos, Surface, grain-boundary and interfacial energies in AI203 and AI203-Sn, AI203-Co systems, J. Mater. Sci. 20 (1985) 3993–4000.
[54] R. Sui, C. Ju, W. Zhong, Q. Lin, Improved wetting of Al2O3 by molten Sn with Ti addition at 973–1273 K, J. Alloy. Compd. 739 (2018) 616–622, https://doi.org/10.1016/j.jallcom.2017.12.350.
[55] M. Molteni, M. Bona, A. Chierichetti, G. Trecordi, E. Gariboldi, Microstructural suitability and stability of AlSi10Mg–Sn plasma coatings for thermal energy storage purposes, Metals 14 (2024), https://doi.org/10.3390/met14121414.
[56] Q. Luo, M. Cong, H. Li, L. Zhu, H. Chen, Q. Li, Mechanism of Fe removal by Sn addition in Al-7Si-1Fe alloy, J. Alloy. Compd. 948 (2023), https://doi.org/10.1016/j.jallcom.2023.169724.
[57] A.R. Farkoosh, D.C. Dunand, D.N. Seidman, Enhanced age-hardening response and creep resistance of an Al-0.5Mn-0.3Si (at%) alloy by Sn inoculation, Acta Mater. 240 (2022), https://doi.org/10.1016/j.actamat.2022.118344.
[58] M.V. Peralta-Martinez, W.A. Wakeham, Thermal Conductivity of Liquid Tin and Indium 1, 2001.
[59] J. Ordonez-Miranda, J.J. Alvarado-Gil, Effect of the pore shape on the thermal conductivity of porous media, J. Mater. Sci. 47 (2012) 6733–6740, https://doi.org/10.1007/s10853-012-6616-7.
[60] F. Cernuschi, S. Ahmaniemi, P. Vuoristo, T. Mäntylä, Modelling of thermal conductivity of porous materials: Application to thick thermal barrier coatings, J. Eur. Ceram. Soc. 24 (2004) 2657–2667, https://doi.org/10.1016/j.jeurceramsoc.2003.09.012.
[61] H. Okamoto, Desk Handbook: Phase Diagrams for Binary Alloys, ASM International, Materials Park, OH, 2000.
[62] A.K. Nayak, W. Oelsen, Quantitative thermal analysis of magnesium-tin alloys by calorimetric measurement for the determination of solidus and liquidus curves, Trans. OfThe Indian Inst. Met. (1969) 53–58.
[63] E. Gariboldi, M. Molteni, D.A. Vargas Vargas, K. Naumenko, Thermo-mechanical response and form-stability of a fully metallic composite phase change material: Dilatometric tests and finite element analysis, Materials Science Engineering A 920 (2025), https://doi.org/10.1016/j.msea.2024.147562.